

RESEARCH

Open Access



MBS_{NRP2}-based ultrasound molecular imaging for early diagnosis of castration-resistant prostate cancer

Na Wang^{1,2†}, Xinzhi Xu^{2†}, Yizhe Zhong^{1,2}, Yujie Wan², Ruixia Hong², Qizhi Wang², Jia Tang², Jiaqi Gong², Hang Zhou^{2*} and Fang Li^{1,2*}

Abstract

Introduction Prostate cancer is one of the most prevalent malignancies in men. Once prostate cancer advances to castration-resistant prostate cancer (CRPC), the 5-year survival rate can decrease to as low as 14 months. However, the current primary diagnostic method, PSA testing, is associated with a lengthy detection cycle, limited accuracy, and delays in identifying disease progression. Consequently, there is an urgent need to develop an imaging technique that enables early and accurate diagnosis of CRPC.

Methods First, immunofluorescence was used to verify that the expression of NRP2 on endothelial cells of neovasculature increased with the progression of prostate cancer. Next, NRP2-modified microbubbles (MBS_{NRP2}) were prepared, and their specific targeting ability to endothelial cells was validated through parallel plate flow experiments. Subsequently, co-culture systems of prostate cancer cells and endothelial cells were established. Based on this, the proangiogenic effect of prostate cancer was systematically explored, and the differential expression of NRP2 was analyzed. A combination of immunofluorescence localization, flow cytometry, western blotting, and angiogenesis assays was used. Finally, in a subcutaneous tumor-bearing mouse model, ultrasound molecular imaging (USMI) was implemented, and the ultrasound contrast intensity of attached MBS_{NRP2} was monitored and quantitatively analyzed.

Results This study confirmed the clear colocalization of NRP2 with CD31 in prostate cancer tissues. Secondly, MBS_{NRP2} exhibited specific binding ability under dynamic conditions to microvascular endothelial cells (HMEC-1). Subsequently, with the progression of CRPC, the expression of NRP2 on HMEC-1 cells gradually increased, accompanied by a significant enhancement in their angiogenic capacity. Lastly, compared with control mice, the USMI signals in tumor-bearing mice from the hormone-sensitive prostate cancer (HSPC), non metastatic, castration-resistant prostate cancer (nmCRPC), and metastatic, castration-resistant prostate cancer (mCRPC) groups were significantly increased. This finding provides a potential new pathway for clinical diagnosis of the development of CRPC.

Conclusion Regarding the progression of prostate cancer, the expression of NRP2 on neovascular endothelial cells gradually increases, potentially serving as a molecular target for early diagnosis of CRPC. The attached MBS_{NRP2}

[†]Na Wang and Xinzhi Xu contributed equally to this work and should be considered as co-first authors.

*Correspondence:

Hang Zhou

zhouh528@163.com

Fang Li

lifang0703@cqu.edu.cn

Full list of author information is available at the end of the article



intensity has significant differences in prostate cancer models at different stages. These findings suggest that ultrasound contrast imaging based on $MB_{S_{NRP2}}$ could be a novel strategy for the early diagnosis of CRPC.

Keywords Ultrasound molecular imaging, Neuropilin 2 (NRP2), Prostate cancer, Targeted microbubbles, CRPC

Introduction

Prostate cancer is the first leading cause of cancer-related new cases and the second leading cause of cancer-related deaths in men worldwide in 2024 [1]. The number of incidences and fatalities is showing an upward trend, posing a severe threat to the health of middle-aged and elderly men. Androgen deprivation therapy (ADT) remains the mainstay of treatment for patients with advanced prostate cancer. However, after an initial favorable response, patients often develop resistance to ADT with resulting tumor progression [2]. NmCRPC is a clinical setting defined as confirmed rising levels of PSA in patients treated with ADT but without detectable metastases on conventional imaging with computerized tomography (CT) and technetium-99m scintigraphy [3]. Delaying the development of metastases in these patients is a key therapeutic goal since metastasis is associated with both morbidity and prostate cancer-specific mortality [4]. The second-generation nonsteroidal androgen receptor inhibitors, such as abiraterone, darolutamide, and enzalutamide, can significantly prolong metastasis-free survival, delay the time to pain progression and the median time to prostate-specific antigen (PSA) progression of patients with castration-resistant prostate cancer (CRPC), substantially reducing the risk of metastasis and death [4–6]. In other words, if prostate cancer is detected early in the non-metastatic stage, allowing for timely adjustment of the treatment plan, the prognosis of the patient can be significantly improved. PSA levels are considered to be the most relevant predictor of progression in nmCRPC [3]. However, due to its extended diagnostic cycle, poor patient compliance, and susceptibility to factors like benign prostatic hyperplasia and prostatitis, the accuracy of PSA diagnosis is low and exhibits significant delay. Currently, PSA is merely a screening tool, and its significance in diagnosing nmCRPC is extremely limited. Furthermore, the absence of clear imaging diagnostic criteria in the non-metastatic stage poses a challenge for diagnosing nmCRPC. This is a crucial issue that urgently requires attention [7].

USMI is an emerging imaging strategy with large potential in cancer detection, which combines the advantages of ultrasound, such as real-time anatomical imaging, with the capabilities of molecular imaging, such as high sensitivity and specificity non-metastatic [8, 9]. Ultrasound imaging has become molecularly

specific with the development of ultrasound contrast agents (UCAs) targeted with ligands such as antibodies or other proteins to detect the expression of cancer-specific molecular markers on the neovascular endothelium [10–12]. Microbubbles remain exclusively within the vascular compartment [13], which makes them particularly well-suited for visualizing molecular markers expressed on the tumor neovascular in various cancers [14]. Notably, angiogenesis plays a crucial role in prostate cancer survival, progression, and metastasis [15, 16]. As resistance to ADT develops in prostate cancer, there are associated changes at the neovascular level, including an increase in microvessel density (MVD), a rise in the proportion of blood vessels around the tumor, and an elevation in the levels of factors related to angiogenesis [17–19]. Therefore, focusing on microvascular changes may offer a viable approach for the early diagnosis of nmCRPC. Molecular markers that are differentially expressed in tumor neovascularization among normal tissues, HSPC, nmCRPC, and mCRPC hold significant importance as potential molecular targets. Currently, prostate cancer-related targets include PSMA, GRPR, and STEAP1, among others, which are overexpressed on the surface of prostate cancer cells but do not affect prostate cancer vascular endothelial cells. Most relevant research has focused on targeted therapy for prostate cancer [20, 21]. Vascular targets, such as VEGFR, lack specific targeting of malignant tumor blood vessels [22].

Neuropilin 2 (NRP2), a VEGFR2 co-receptor, is involved in tumor metastasis and is correlated with poor prognosis [23]. NRP2 was discovered as a novel tumor neovasculature-associated marker differentially expressed in pancreatic neuroendocrine tumors, vascular malformations, and head and neck cancer [24–26]. Recently, the NRP2 protein was shown to be expressed in human prostate cancer tissues [22]. NRP2 is becoming increasingly recognized as a candidate target for suppressing pathologies typified by uncontrolled vascular expansion, such as cancer, which would make NRP2 an attractive novel molecular imaging target for prostate cancer detection [27, 28]. In summary, this study intends to modify microbubbles with NRP2 targeting and verify through *in vitro* and *in vivo* studies whether it can serve as an effective molecular imaging method for predicting prostate cancer progression.

Materials and Methods

Study design

As shown in Fig. 1, firstly, at the cellular and tissue levels, verify whether the expression of NRP2 is upregulated in the endothelial cells of neovascularization during the progression of PCa, and conduct an in-depth exploration of whether this upregulation has a positive correlation with the degree of CRPC. Secondly, MBs_{NRP2} can be prepared using the biotin-avidin system. Simulating the conditions of physiological shear stress through a parallel plate flow chamber experiment to evaluate the specific targeting and binding efficiency of MBs_{NRP2} to vascular endothelial cells. Subsequently, on the premise of ensuring the safety of MBs_{NRP2} , we carry out USMI experiments in a subcutaneous tumor-bearing mouse model

using MBs_{NRP2} . By monitoring and quantitatively analyzing the changes in the echo intensity of the attached MBs_{NRP2} specifically bound to the vascular endothelium, verify the differences in the echo intensity of USMI of PCa at different stages. Finally, conduct an in-depth analysis of the USMI data obtained from the subcutaneous tumor-bearing model, collect quantitative parameters, and perform statistical analysis. Based on this, construct a CRPC diagnostic model.

Validation of NRP2 expression in human prostate tissues

Collection of human prostate tissues

Human prostate tissue samples were obtained retrospectively to represent a range of normal, HSPC, nmCRPC, and mCRPC. A total of 20 samples were

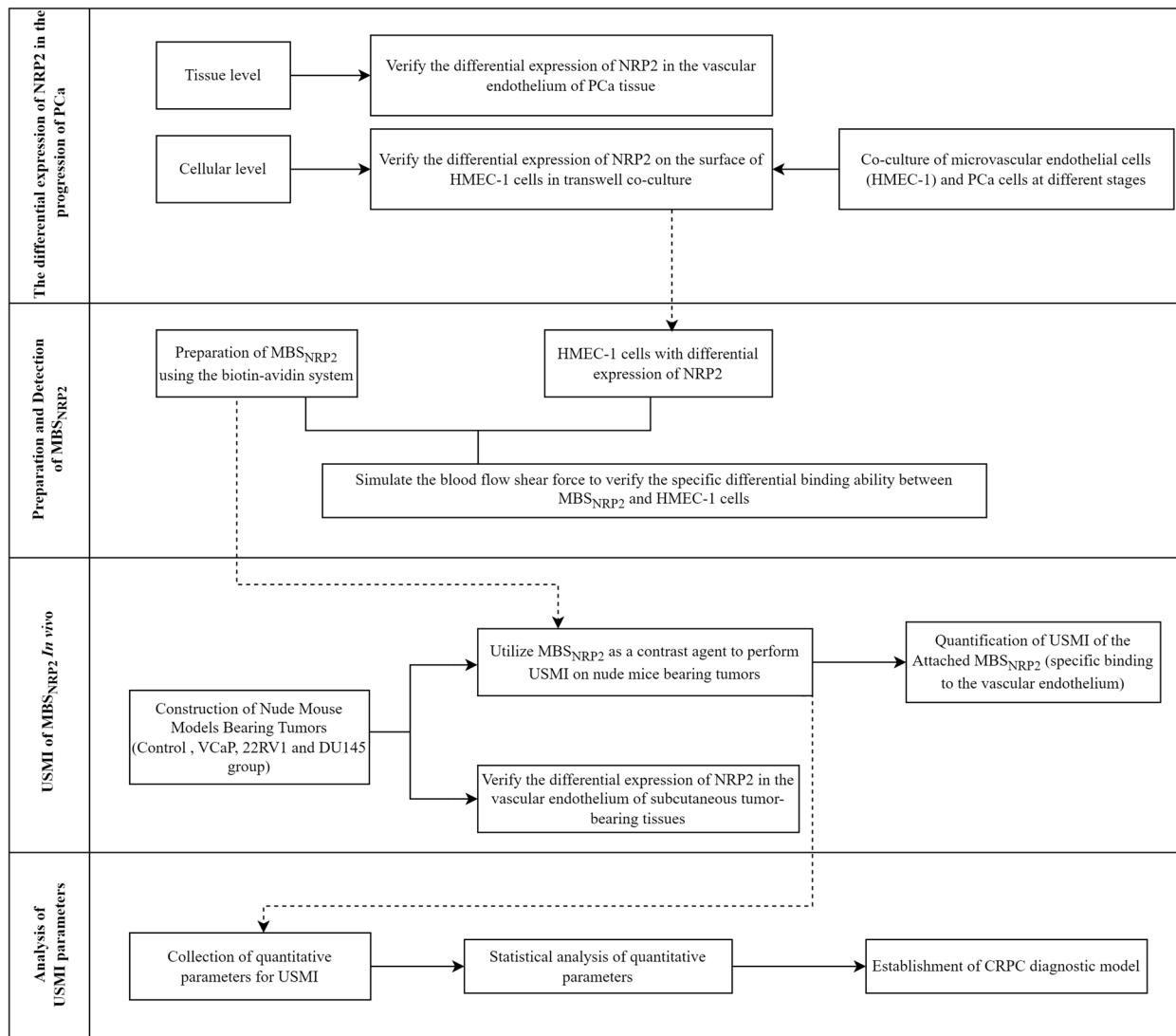


Fig. 1 Technical roadmap for the diagnosis of nmCRPC by USMI based on MBs_{NRP2}

obtained, including 5 normal prostate tissue, 5 HSPC, 5 nmCRPC, and 5 mCRPC. Benign tissues adjacent to prostate cancer were used as intra-individual benign control tissues. Our study obtained informed consent from the patients and was approved by the Ethics Committee of the Chongqing University Affiliated Cancer Hospital, with the ethics approval number CZLS2025019-A (Table 1).

Immunofluorescence localization staining of NRP2 in human prostate tissues

All samples were obtained from biopsies or surgical resections. Endothelial cells were labeled with anti-mouse CD31 antibody (3528, CST) and anti-rabbit Neuropilin- 2 antibody (3366, CST), followed by secondary Alexa Fluor 647-coupled goat anti-mouse IgG (4410, CST) and Alexa Fluor 488-coupled goat anti-rabbit IgG (4412, CST). Stained sections of a maximum number of tumor samples and normal prostate tissue were imaged on a STELLARIS 5 confocal microscope (Leica) on the same day to allow for relative quantification of fluorescence staining. Fluorescence images were analyzed using LAS X software. The endothelial presence of NRP2 was indicated by co-registration of fluorescence signals for NRP2 and CD31.

Table 1 Information on human samples

	Age	Sex	Gleason score	TNM staging
Normal 1	69	Male	-	-
Normal 2	48	Male	-	-
Normal 3	79	Male	-	-
Normal 4	73	Male	-	-
Normal 5	61	Male	-	-
HSPC 1	77	Male	4 + 3 = 7	T ₂ N ₀ M ₀
HSPC 2	76	Male	3 + 3 = 6	T _{1b} N ₀ M ₀
HSPC 3	78	Male	3 + 4 = 7	T _{2a} N ₀ M ₀
HSPC 4	67	Male	4 + 3 = 7	T _{2a} N ₀ M ₀
HSPC 5	61	Male	4 + 3 = 7	T _{2a} N ₀ M ₀
nmCRPC 1	86	Male	3 + 5 = 8	T ₃ N ₁ M ₀
nmCRPC 2	71	Male	5 + 4 = 9	T ₄ N ₁ M ₀
nmCRPC 3	84	Male	5 + 4 = 9	T _{3a} N ₁ M ₀
nmCRPC 4	77	Male	5 + 5 = 10	T _{2c} N ₁ M ₀
nmCRPC 5	76	Male	4 + 4 = 8	T ₄ N ₁ M ₀
mCRPC 1	45	Male	5 + 4 = 9	T _{4a} N ₁ M ₁
mCRPC 2	54	Male	4 + 4 = 8	T _{3a} N ₁ M _{1b}
mCRPC 3	76	Male	5 + 4 = 9	T _{3b} N ₁ M _{1b}
mCRPC 4	77	Male	5 + 4 = 9	T ₄ N ₁ M _{1b}
mCRPC 5	79	Male	4 + 4 = 8	T _{3b} N ₁ M _{1b}

Preparation of MBs_{NRP2} and validation of its specific binding to vascular endothelial cells.

Preparation and analysis of MBs_{NRP2}

Commercially available streptavidin-coated microbubbles (Bracco Suisse SA, Geneva, Switzerland) were used to generate MBs_{NRP2} and MBs_{Control}. Each vial of lyophilized streptavidin-coated microbubbles was suspended in 1 mL of sterile saline (0.9% sodium chloride) according to the manufacturer's protocol. MBs_{NRP2} were prepared using streptavidin–biotin binding chemistry to target rabbit anti-NRP2 biotin-conjugated antibodies (bs- 10241R-Bio, Bioss). The size and zeta potential of MBs_{NRP2} were measured using 90Plus PALS (Brookhaven). The number of antibodies binding to the microbubble surface was determined by FCM and immunofluorescence after incubating the targeted microbubbles with fluorescein-conjugated anti-biotin antibodies.

Flow Chamber assessment of MBs_{NRP2} binding specifically

The binding specificity of MBs_{NRP2} to the target NRP2 was assessed in co-cultured HMEC- 1 cells under flow shear stress conditions simulating blood flow using a flow chamber experimental setup. 1×10^6 co-cultured HMEC- 1 cells were grown on a parallel plate flow chamber (μ -Slide I Luer, Abidi, Germany) for 6 h. A syringe infusion and withdrawal pump (CP- 1100, SLGO) were used to maintain the flow rate of 0.6 mL/min [29]. The following order was maintained for running each type of microbubble suspension: PBS for 2 min, 1×10^8 of MBs_{NRP2} in PBS for 4 min, and PBS for 2 min. The slides were immediately imaged using a digital microscope camera, and the number of MBs_{NRP2} specifically attached to the endothelial cells was counted.

Validation of NRP2 expression in HMEC- 1 cells co-cultured with prostate cancer cells

HMEC- 1 cells co-cultured with prostate cancer cells

1×10^6 DU145 prostate cells were seeded into a transwell insert of 0.4 μ m (Labsselect, Hefei, China) for co-culture with 1×10^6 endothelial cells (HMEC- 1) seeded in the 6-well plates. The cultivation of 22RV1 and VCaP cells was also conducted under the same conditions mentioned above. The endothelial cells were harvested for use 24 h after seeding. DU145 is a cell line derived from mCRPC, 22RV1 represents an nmCRPC cell line, and VCaP is a cell line of HSPC. Normal vascular endothelial HMEC- 1 cells were obtained from the National Collection of Authenticated Cell Cultures (Shanghai, China). Prostate cancer cell lines DU145, 22RV1, and VCaP were purchased from Zhong Qiao Xin Zhou Biotechnology (Shanghai, China) and were cultured in a humidified incubator maintained at 37 °C with 5% CO₂. All cells

were maintained in medium (Gibco, Shanghai, China) supplemented with 10% fetal bovine serum (FBS; Viva-Cell, Shanghai, China) and 1% penicillin/streptomycin (Pricella, Wuhan, China), following the manufacturer's instructions.

Immunofluorescence localization staining of NRP2 in neovascular endothelial cells

To verify the expression of NRP2 on neovascular endothelial cells, all HMEC-1 cells obtained through co-culture were subjected to immunofluorescence staining and analysis, using the same methodology as for human prostate tissue sections. Endothelial cells were labeled with anti-mouse CD31 antibody (3528, CST) and anti-rabbit Neuropilin-2 antibody (3366, CST), followed by secondary Alexa Fluor 647-coupled goat anti-mouse IgG (4410, CST) and Alexa Fluor 488-coupled goat anti-rabbit IgG (4412, CST). Stained sections of a maximum number of tumor samples and normal prostate tissue were imaged on a CLSM on the same day to allow for relative quantification of fluorescence staining. Fluorescence images were analyzed using LAS X software. The endothelial presence of NRP2 was indicated by co-registration of fluorescence signals for NRP2 and CD31.

Flow cytometry

Based on the co-culture protocol outlined above, all HMEC-1 cells were incubated with primary anti-rabbit Neuropilin-2 antibody (3366, CST) for 40 min at 4 °C, followed by incubation with secondary Alexa Fluor 488-conjugated goat anti-rabbit IgG (4412, CST) for 20 min at 4 °C in the dark. The fluorescence intensity of the samples was then Non-tumor-bearing detected and analyzed using the Novocyte Advanteon (Agilent).

Western blotting

Based on the co-culture protocol mentioned above, all HMEC-1 cells obtained were lysed with RIPA buffer (Beyotime Biotechnology, China) containing protease inhibitor (Beyotime Biotechnology, China) on ice. The concentration of total protein was quantified using a BCA Protein Assay Kit (Beyotime Biotechnology, China). Equivalent amounts of total cellular protein were resolved by 10% sodium dodecyl sulfate–polyacrylamide gel electrophoresis (SDS–PAGE) and transferred onto polyvinylidene difluoride (PVDF) membranes. The membranes were blocked with 5% bovine serum albumin (BSA) for 2 h at room temperature, incubated with primary anti-rabbit Neuropilin-2 antibody (3366, CST) overnight at 4 °C, anti-rabbit Neuropilin-2 antibody (3366, CST) for 1 h. Finally, the membranes were visualized and measured by an ECL system (Beyotime Biotechnology, China), followed by imaging using a BIO-RAD system.

Tube formation assay

Based on the co-culture protocol outlined above, HMEC-1 cells were seeded at a density of 1×10^5 cells/ml in a 6-well plate. Similarly, DU145, 22RV1, and VCaP cells were seeded at a density of 1×10^5 cells/ml in a 0.4 μ m transwell insert (Labselect, Hefei, China), with a control group included. After incubating the seeded cells in a constant-temperature incubator for 6 h, tube formation by HMEC-1 cells was imaged using a BX53 digital microscope camera (Olympus). For each group, three parallel controls were set up, and five random optical fields were selected to quantify the number of tube formations using ImageJ.

Validation and analysis of NRP2 expression in tumor-bearing mice

NRP2-targeted USMI in vivo

1. Mouse models: VCaP, 22RV1, and DU145 cells (1×10^7) were injected subcutaneously into the lower right abdomen of 5-week-old male BALB/c nude mice, serving as animal models for HSPC, nmCRPC, and mCRPC. The prostate location of non-tumor-bearing mice was determined through pathological confirmation, followed by subsequent USMI, immunofluorescence, and immunohistochemistry. The tumor reaches a volume of 1000 mm³, it will be used for targeted ultrasound molecular imaging. All procedures involving the use of laboratory animals were approved by the Institutional Administrative on Laboratory Animal Care. The experimental animals used in this study were purchased from Jiangsu Jicui Pharmaceutical Biology Limited Company. All procedures involving the use of experimental animals were approved by the Ethics Committee of the Chongqing University Affiliated Cancer Hospital, with the ethics approval number CZLS2024241-A. At the end of the experiment, the mice were euthanized by cervical dislocation to minimize their pain and stress.

2. Imaging protocol: Prostate tumor-bearing nude mice ($n = 18$) and non-tumor-bearing mice ($n = 6$) were imaged. Tumors were imaged when they reached approximately 10 mm in diameter. During imaging, mice were under anesthesia with tribromoethanol (AiBei Biotechnology, China) and kept warm using a heated stage and a heat lamp. For coupling of the ultrasound transducer, pre-warmed gel was applied on the skin of the regions to be imaged. The imaging system Aplio i800 (Canon Medical Systems Corporation, China), in combination with the i18LX5 transducer, was used for all acquisitions. Scanning through the tumor tissue in ultrasound B-mode, the 2D cross-section showing the tumor's neovascularization at its biggest diameter was identified and selected for image acquisition. The same batch of MBs was used for all

imaging studies in vivo. A total of 1×10^7 MBs_{NRP2}, dissolved in 100 μ L of PBS, was injected into the tail vein using a 25G needle via an insulin syringe. After the injection of MBs_{NRP2}, the targeted microbubbles fully bind to the neovascular endothelium of prostate cancer. 2 min later, USMI is performed on the tumor or normal prostate. The imaging parameters are set to a mechanical index of 0.22, a dynamic range of 60 dB, and a frame rate of 13 frames per second. Within 10 s, a total of 130 imaging frames are collected. The ultrasound microbubble echo intensity represents the combined signals from both freely MBs_{NRP2} and attached MBs_{NRP2}. "Attached MBs_{NRP2}" refers to MBs_{NRP2} that specifically bind to the neovascular endothelium of prostate cancer. Then, initiating the continuous high-power destructive pulse blasting (Flash) program, set the transmission power at 100%, the mechanical index at 0.98, and the duration at 1 s. All the MBs_{NRP2} within the observed section are instantaneously destroyed by the powerful pulse energy. Within 10 s, a total of 130 imaging frames are collected in the same way to precisely capture the acoustic signals generated by the freely circulating MBs_{NRP2}. Finally, the destruction-replenishment method was used to quantify MBs_{NRP2} by comparing the pre-burst signal from both freely circulated and attached MBs_{NRP2} with the replenishment signal from freely circulated MBs_{NRP2} acquired immediately after a destructive pulse. Between acquisitions of different images of MBs_{NRP2} in the same mouse, a lag time of at least 30 min was included to allow for wash-out of the MBs_{NRP2} [8, 10, 30].

In terms of image analysis, we utilize the SonoLIVER software. First, to standardize the images, we adjust the display intensity and color to be consistent. Second, the built-in algorithms of the SonoLIVER software can effectively reduce noise interference and motion artifacts in the images. We only need to perform calibration operations. Finally, we manually and randomly select three regions of interest (ROI) and calculate the average value of the USMI echo intensities of these three regions to ensure the reliability of the image data [31–33].

3. Imaging data analysis: During the progression of CRPC, tumor cells release angiogenesis factors, which give rise to a large number of new blood vessels with irregular shapes and tortuous courses, distinctly different from normal blood vessels. Thanks to the abundant new blood vessels and relatively fast blood flow during contrast-enhanced ultrasound, CRPC lesions fill rapidly in the arterial phase. The contrast agent surges in vigorously, immediately increasing the echo, and the subsequent perfusion is also higher than that of normal tissues [34]. The ligands on the surface of CRPC have strong binding ability. After binding specifically to the targeted

microbubbles, they will aggregate in large quantities at the target site, reducing the possibility of being cleared by the blood circulation [35].

Given all the above characteristics, we have deeply analyzed the relevant parameters that can reflect the perfusion and washout situations, including peak intensity (PI), time to peak intensity (TTP), rise time (RT), rise slope (RS), area under the time-intensity curves (AUC), area under the wedge in curves (winAUC), wedge in rate (winR), fall half time (FHT), mean Transit Time (mTT), fall slope (FS), fall time (FT), area under the wedge out curves (woutAUC), and wedge out rate (WoutR). These are important parameters for precisely quantifying and evaluating key hemodynamic characteristics of the contrast agent within the lesion, including the peak enhancement level, the speed of reaching the peak, the rising rate, the overall perfusion degree, and the speed of decline [34, 36].

Logistic regression analysis was performed to determine the significant features associated with malignancy. All variables with $P < 0.05$ in the univariable logistic regression analysis were incorporated into the multivariable logistic regression analysis. $P < 0.05$ was considered statistically significant. All statistical analyses were performed using SPSS 27.0 (IBM Corp).

Immunofluorescence localization staining and analysis of NRP2 expression in tumor-bearing mice

To verify the expression of NRP2 on neovascular endothelial cells, all tissue samples obtained through subcutaneous tumors were subjected to immunofluorescence staining and analysis, using the same methodology as for human prostate tissue sections. Endothelial cells were labeled with anti-mouse CD31 antibody (3528, CST) and anti-rabbit Neuropilin-2 antibody (3366, CST), followed by secondary Alexa Fluor 647-coupled goat anti-mouse IgG (4410, CST) and Alexa Fluor 488-coupled goat anti-rabbit IgG (4412, CST). Stained sections of a maximum number of tumor samples and normal prostate tissue were imaged on a STELLARIS 5 confocal microscope (Leica) on the same day to allow for relative quantification of fluorescence staining. Fluorescence images were analyzed using LAS X software. The endothelial presence of NRP2 was indicated by co-registration of fluorescence signals for NRP2 and CD31.

Immunohistochemistry (IHC) staining and analysis of NRP2 expression in tumor-bearing mice

IHC was performed on standard serial 5 μ m sections of paraffin-embedded prostate tissues using the Leica HistoCore MULTICUT semi-automatic rotary slice. Endothelial cells were labeled with anti-mouse CD31 antibody (3528, CST) and anti-rabbit Neuropilin-2 antibody

(3366, CST), followed by secondary labeling with Goat anti-mouse IgG(H + L), HRP Conjugated(LF101, Epizyme Biotech) and Goat anti-rabbit IgG(H + L), HRP Conjugated(LF102, Epizyme Biotech). Antibodies to both CD31(to confirm the presence of tumor vessels) and NRP2 were used on the same platform. Slides were imaged using a VS120 digital slide scanner (Olympus). Adjacent CD31-stained sections were used as anatomical guides to locate the endothelial cells of tumor-associated neovascularization to determine the presence of tumor blood vessels. The ImageJ software was used to count the number of vascular endothelial positive cells and total cells in each field of view, and then the percentage of positive cells in the total cells was calculated.

Statistical methods

Statistical analysis of the data was performed using SPSS 27.0. The experimental data were all expressed in the form of mean \pm standard deviation (mean \pm SD), and independent sample T-tests or analysis of variance were used for processing. If $P < 0.05$, it indicates that there is a statistically significant difference between the data.

Results

NRP2 Expression in Vascular Endothelium Gradually Increases with Prostate Cancer Progression

As shown in Fig. 2a, the study design aimed to validate NRP2 as a molecular imaging diagnostic target in the blood pool for prostate cancer. The study collected and analyzed samples from patients at different stages of prostate cancer. A total of four key stages in prostate cancer progression were included: normal prostate, HSPC, nmCRPC, and mCRPC ($n = 5$). These samples were stained for NRP2 and CD31(a marker of neovascularization). The colocalization relationship between NRP2 and CD31 was analyzed. The results showed that regardless of the stage of prostate cancer, NRP2 demonstrated good colocalization with CD31, strongly suggesting its potential as a target for blood pool contrast agents(Fig. 2b). Next, a semi-quantitative analysis of NRP2 fluorescence intensity across different stages of prostate cancer was conducted. The results indicated that as prostate cancer progressed, the expression of NRP2 increased significantly (Normal vs HSPC vs nmCRPC vs mCRPC: 11.39 vs 15.65 vs 26.63 vs 27.71, $p < 0.05$) (Fig. 2c). In summary, as prostate cancer progresses, the expression of NRP2 on the corresponding vascular endothelium also increases significantly, especially during the transition from HSPC to nmCRPC. This strongly suggests the possibility of NRP2 serving as a molecular target for the precise diagnosis of prostate cancer progression, especially the early detection of castration resistance.

Preparation and Validation of MBs_{NRP2}

As the study design illustrates in Fig. 3a, MBs_{NRP2} was prepared by MBs_{Control} with a biotin-avidin system. MBs_{NRP2} exhibits a circular morphology with a uniform particle size, and the average particle size is 1157 nm (Fig. 3b). The morphology of MBs_{NRP2} remained largely unchanged, suggesting that the loading of NRP2 did not disrupt the structure of microbubbles. From Fig. 3c, the negative charge of NRP2 contributed to a zeta potential of -10.3 mV for MBs_{NRP2}, which was significantly lower than the zeta potential of -8.3 mV for MBs_{Control}. Interestingly, the zeta potential value of MBs_{NRP2} was slightly lower than that of MBs_{Control} due to the negative charge on the NRP2 antibody. This observation suggests that the NRP2 antibody was successfully loaded onto the MBs_{Control}. As shown in Fig. 3d, the peaks located from 820 cm^{-1} to 1161 cm^{-1} , and 2890 cm^{-1} in the FTIR spectrum of MBs_{NRP2} matched well with those of the biotin-avidin system [37, 38]. CLSM was employed to investigate the specific binding of NRP2 mAb to MBs_{Control}, as illustrated in Fig. 3e. These results were corroborated by flow cytometry data, indicating that the binding rate of the NRP2 antibody reached 86.1%, as depicted in Fig. 3f. Altogether, these data strongly indicate that the MBs_{NRP2} has been successfully prepared. Microbubbles targeted to NRP2 molecular epitopes present on vascular endothelial cells were prepared using a biotin-avidin system.

NRP2 Expression in HMEC- 1 Cells Gradually Increases with Co-culture with Prostate Cancer Cells

To verify the differential expression and vascular localization of NRP2, as illustrated in Fig. 4b, the study cocultured prostate cancer cells DU145 (indicating mCRPC), 22RV1 (indicating nmCRPC), and VCaP (indicating HSPC) at different stages with endothelial cells HMEC-1. CD31 and NRP2 show distinct co-localization on the plasmalemma across all groups (Fig. 4a), guided by vascular marker CD31 staining. Weak fluorescence of NRP2 was observed in the plasmalemma of the control group(mean fluorescence signal intensity, 10.73a.u.), which gradually increased with the VCaP group(mean fluorescence signal intensity, 14.12a.u.), the 22RV1 group(mean fluorescence signal intensity, 18.21a.u.) and the DU145 group(mean fluorescence signal intensity, 25.01a.u.) (Fig. 4c). We applied immunofluorescence localization and demonstrated NRP2 expression and its co-localization with CD31 in the tumor vascular endothelium.

To determine whether prostate cancer cells promote the expression of NRP2 on the surface of endothelial cells (HMEC- 1), we co-cultured HMEC- 1 cells with prostate cancer cells and evaluated the expression of

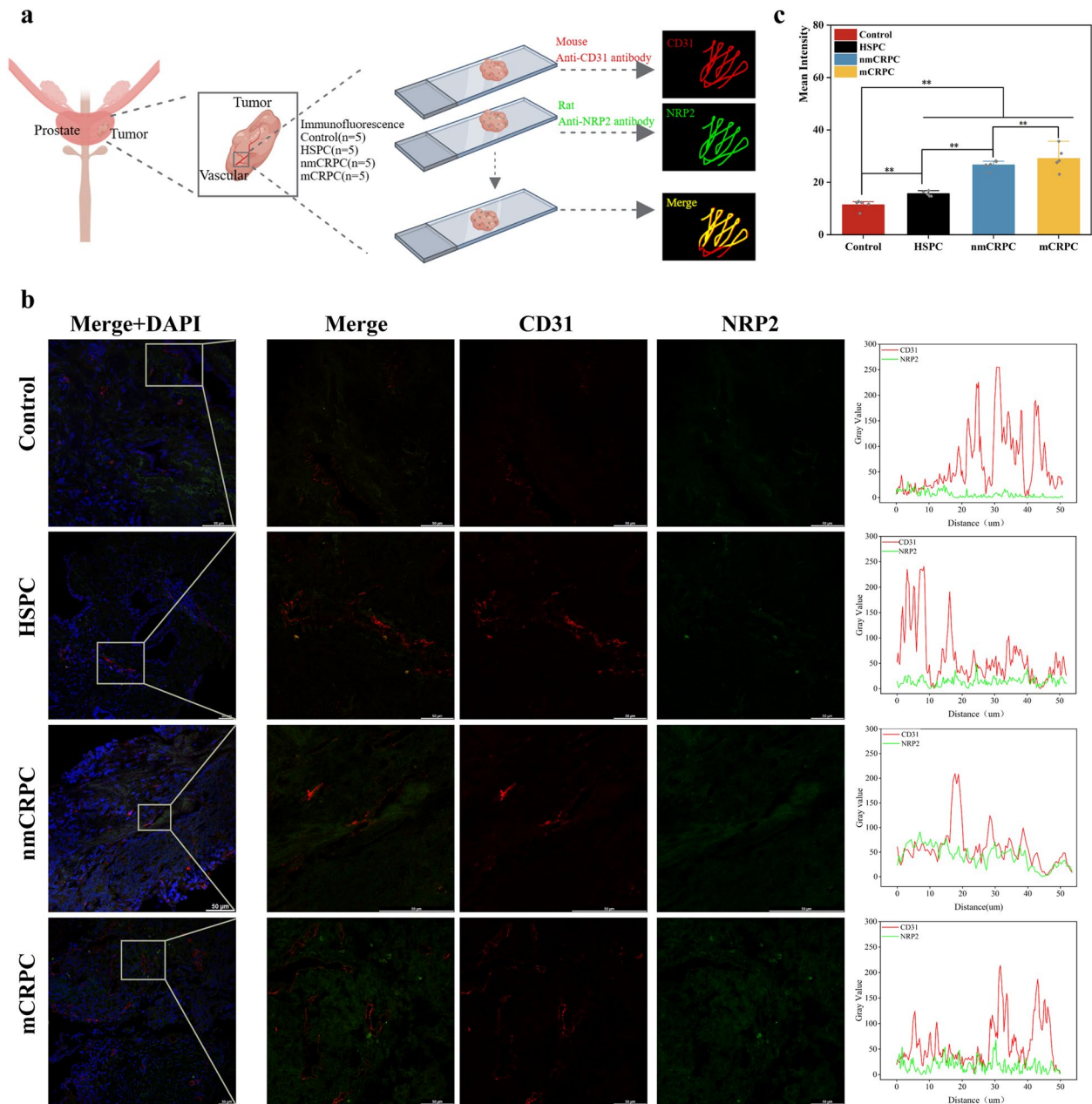


Fig. 2 **a** Study design for immunofluorescence localization staining. **b** Confocal Laser Scanning Microscope (CLSM) images and colocalization analysis for immunofluorescence localization staining of CD31 and NRP2 in human prostate cancer tissues. **c** Fluorescence intensity quantification of NRP2. $n = 5$ samples per group; *, $p < 0.05$; **, $p < 0.01$; ***, $p < 0.005$; error bars present SD

NRP2 protein via western blot analysis (Fig. 4d). Compared to normal control HMEC-1 cells, HMEC-1 cells exhibited a graded increase in NRP2 protein expression, with the smallest elevation seen in response to VCaP cells, followed by a more significant rise with 22RV1 cells, and the most pronounced increase observed in the presence of DU145 cells. These results were corroborated by flow cytometry data, revealing

a distinct pattern of fluorescence intensity in HMEC-1 cells upon interaction with various cell lines. Compared to control HMEC-1 cells, HMEC-1 cells exhibited the most robust fluorescence when stimulated by DU145 cells, a moderate intensity when co-cultured with 22RV1 cells, and a weaker signal in the presence of VCaP cells, as depicted in Fig. 4e. That is to say, under the stimulation of prostate cancer cells,

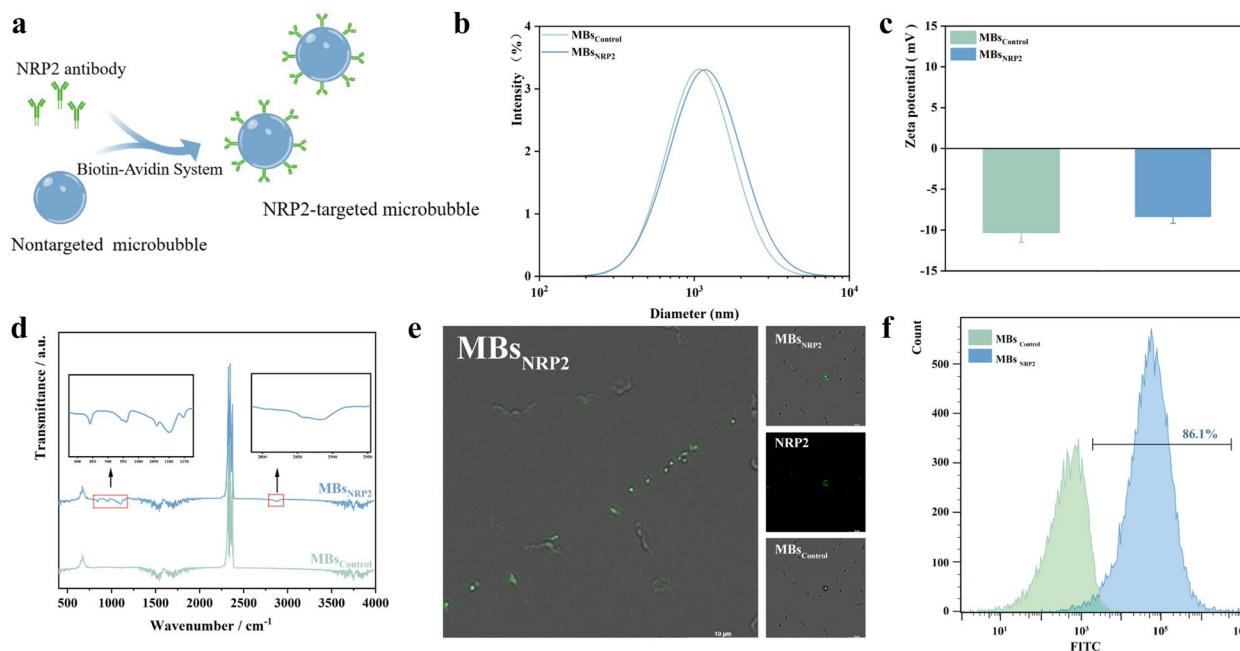


Fig. 3 **a** Schematic diagram of the synthesis of MBs_{NRP2} . **b** Size of $MBs_{Control}$ and MBs_{NRP2} . **c** Zeta Potential of $MBs_{Control}$ and MBs_{NRP2} . **d** FTIR spectra of $MBs_{Control}$ and MBs_{NRP2} . **e** CLSM images of $MBs_{Control}$ and MBs_{NRP2} . **f** Binding rate of MBs_{NRP2}

the expression of NRP2 gradually increases. There are significant differences in NRP2 expression on the surface of vascular endothelial cells as the disease progresses from the stage of HSPC to nmCRPC. This suggests that NRP2 has the potential to be a promising biomarker for early and accurate diagnosis of nmCRPC.

Based on the verification that the expression of NRP2 on the surface of endothelial cells gradually increases under the influence of prostate cancer cells, the study aimed to validate the angiogenic potential of these diverse prostate cancer cell types. We assessed the ability of prostate cancer cells to induce endothelial tube formation and demonstrated that the presence of prostate cancer cells enhanced the tube formation capability of HMEC-1 cells (Fig. 4f). The number of branches formed by control HMEC-1 cells was 31.83. As the prostate cancer cells differentiated into VCaP cells (mean number of branches: 87.3), 22RV1 cells (mean number of branches: 101.17), and DU145 cells (mean number of branches: 141.50), the quantification of tube formation gradually increased (Fig. 4g). In conclusion, as prostate cancer cells progress from normal to nmCRPC, they induce an increase in NRP2 expression on endothelial cells and enhance their angiogenic potential. This significant difference in NRP2 expression across different stages suggests that it could be a valuable tool for early and accurate diagnosis of CRPC.

Verifying the feasibility of USMI using a flow chamber

The parallel-plate flow chamber experiment employs a chamber formed between two parallel plates, where a syringe pump injects liquid into the chamber with controlled force to replicate the blood flow environment within the body. In this study, this setup is utilized to simulate the specific binding of MBs_{NRP2} to NRP2 on the surface of vascular endothelial cells under normal physiological blood flow shear conditions, which holds great significance for targeting USMI [39, 40]. Flow chambers were used to plate HMEC-1s and the number of attached MBs_{NRP2} was counted under a shear stress of 0.6L/min [29] (Fig. 5a). At the same shear stress, there were a few permanent attachments of control HMEC-1 cells (mean number of attached MBs_{NRP2} :4.33), several permanent attachments of HMEC-1 cells subjected to VCaPs (mean number of attached MBs_{NRP2} :5.33), many permanent attachments of HMEC-1 cells subjected to 22RV1s (mean number of attached MBs_{NRP2} :7.17) and Countless permanent attachments of HMEC-1s subjected to DU145s (mean number of attached MBs_{NRP2} :14.33) (Fig. 5b and 5c) ($p < 0.05$). This study confirmed the nmCRPC group exhibits a 1.35-fold increase in the number of attached MBs_{NRP2} compared to the HSPC group. Likewise, as nmCRPC progresses to mCRPC, there is a 2.00-fold increase in the number of attached MBs_{NRP2} . Consequently, the notable difference in NRP2 expression may offer a significant advantage in predicting the onset

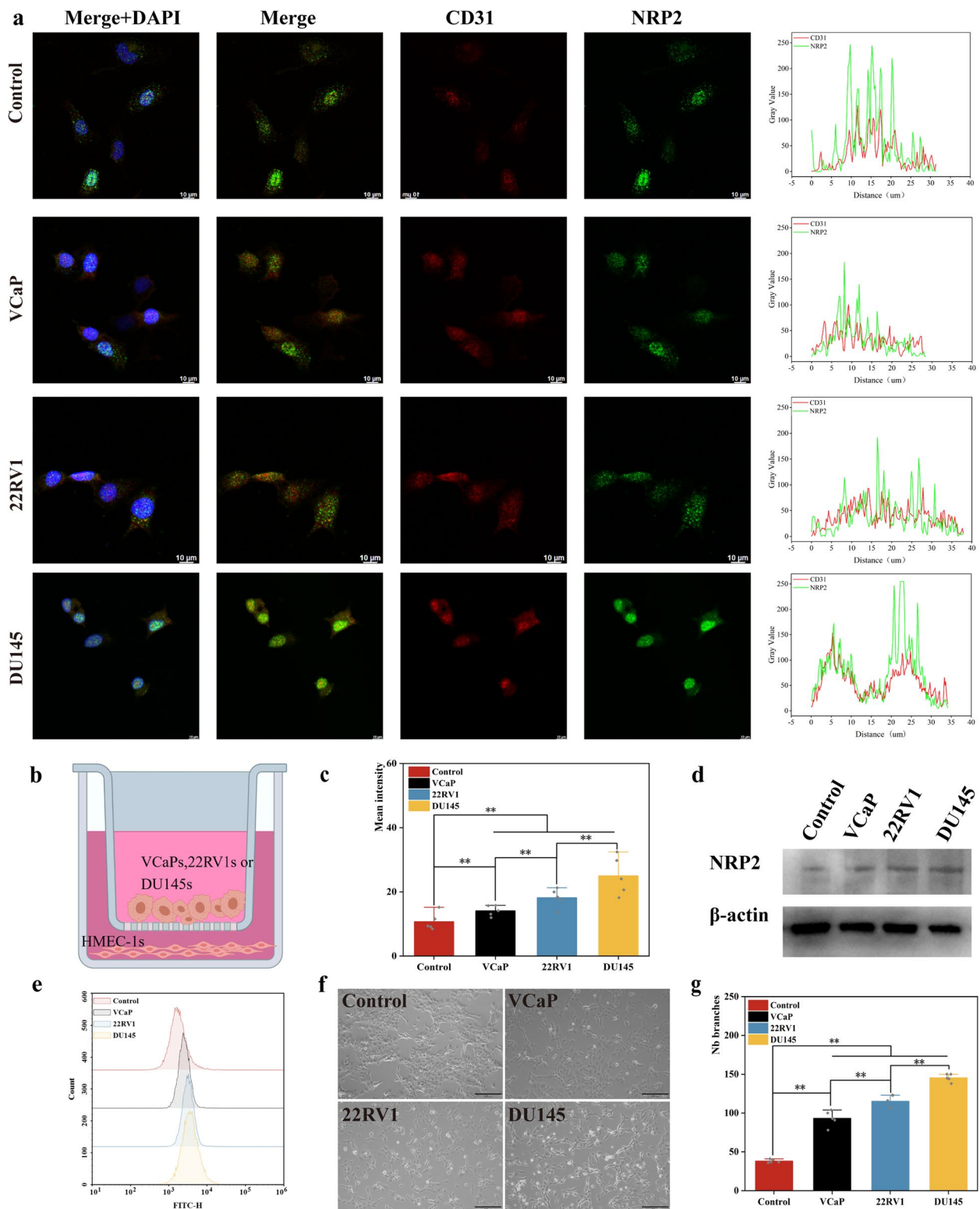


Fig. 4 **a** CLSM images and colocalization for immunofluorescence localization staining of CD31 and NRP2. **b** Schematic diagram of the transwell co-culture. **c** Fluorescence intensity quantification of NRP2. **d** NRP2 expression was depleted in HMEC-1 cells using different prostate cancer cell lines as stimuli. β-actin was used as a loading control. **e** Flow cytometric analyses of HMEC-1 cells exposed to different prostate cancer cell lines. **f** Prostate cancer cells exhibited the ability to promote tube formation in endothelial cells. **g** Quantification of tube formation exposed to different prostate cancer cells. $n = 5$ samples per group; *, $p < 0.05$; **, $p < 0.01$; ***, $p < 0.005$; error bars present SD

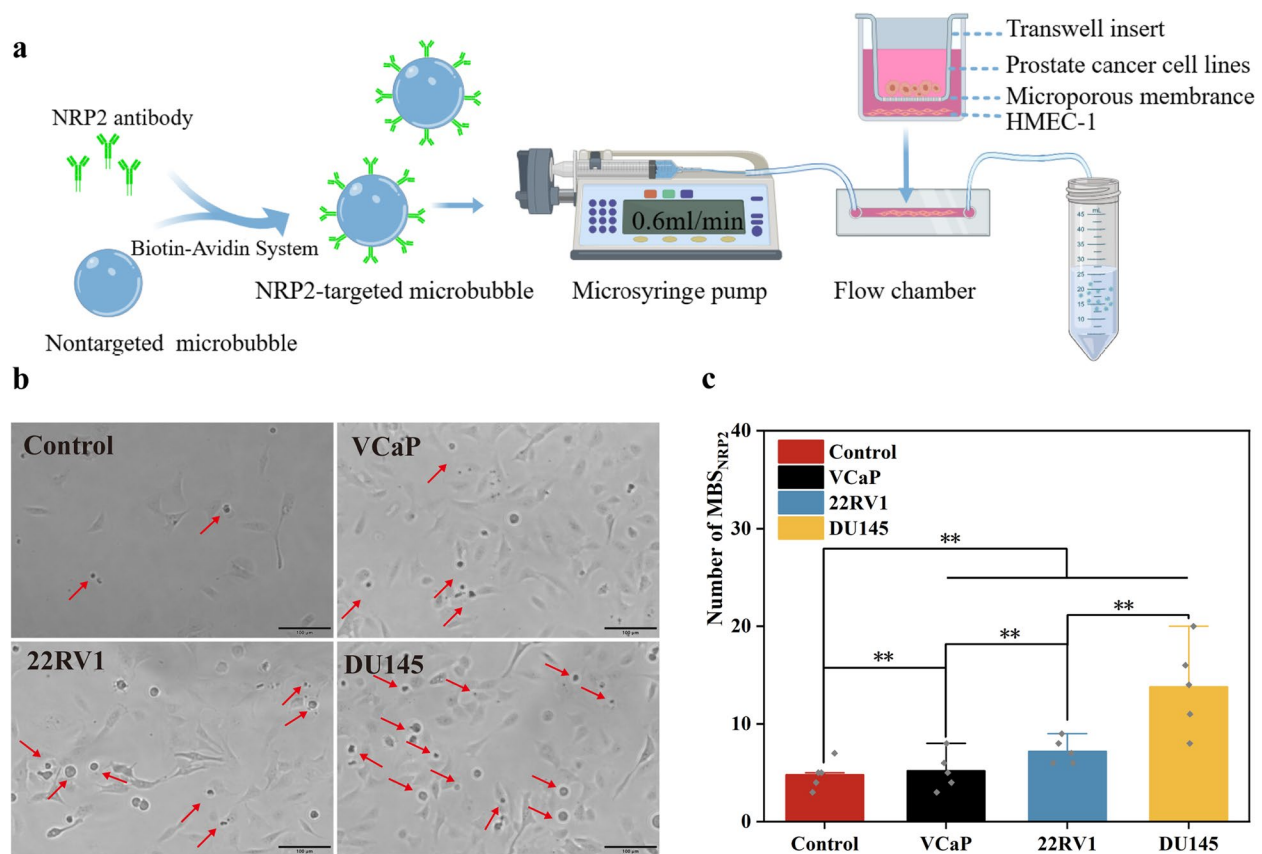


Fig. 5 **a** Study design for the Flow Chamber experiment. **b** MBs_{NRP2} binding on control HMEC-1 cells and HMEC-1 cells exposed to prostate cancer cells (VCaP cells, 22RV1 cells, and DU145 cells) under shear stress (0.6 mL/min). **c** Quantification of MBs_{NRP2} binding to HMEC-1 cells in a single field of view. $n = 5$ samples per group; *, $p < 0.05$; **, $p < 0.01$; ***, $p < 0.005$; error bars present SD

and metastasis of CRPC, thereby laying a solid theoretical foundation for the early diagnosis of nmCRPC using in vivo USMI.

NRP2-Targeted USMI for Diagnosis of nmCRPC In Vivo

To differentiate the acoustic signal arising from attached MBs_{NRP2} or from freely circulated MBs_{NRP2} in the bloodstream, principles of ultrasound-induced microbubble destruction and replenishment were utilized [8]. For this purpose, MBs_{NRP2} were injected intravenously via the tail

vein and allowed to attach to NRP2 on the neovasculature. This was followed by a 1-s continuous high-power destructive pulse, which destroyed all MBs_{NRP2} within the beam of elevation. Another ultrasound contrast signal from the freely circulated MBs_{NRP2} was acquired (Figs. 6a and 6b). The ultrasound contrast signal of attached MBs_{NRP2} is obtained by subtracting the ultrasound contrast signal of freely circulated MBs_{NRP2} from the signal of all MBs_{NRP2} (Fig. 6d). As shown in Figs. 6c and 6e, the ultrasound contrast signal of attached MBs_{NRP2} obtained

(See figure on next page.)

Fig. 6 **a** Study design for contrast ultrasound imaging of a mouse. **b** Study design for ultrasound-induced microbubble destruction and replenishment. **c** B-mode images from tumor-bearing mice and non-tumor-bearing mice; USMI images obtained with all MBs_{NRP2} and freely circulated MBs_{NRP2} before and post the destructive pulse and in tumor-bearing mice and non-tumor-bearing mice. The image panel presents ultrasound B-mode images in grey (upper row) and the respective contrast-enhanced ultrasound image in brown (lower row) including the color-coded USMI dTE signal distribution ((pre-burst)—(post-burst)) in the region of interest (green contour), a local area of the tumor (blue contour), and reference region for USMI (yellow contour). **d** Study design for attached MBs_{NRP2}. **e** Quantification of attached MBs_{NRP2}. **f** CLSM images and colocalization for immunofluorescence localization staining of CD31 and NRP2 in tumor-bearing mice and non-tumor-bearing mice. **g** Fluorescence intensity quantification of NRP2 in tumor-bearing mice and non-tumor-bearing mice. **h** Fluorescence intensity quantification of NRP2 expression in tumor-bearing mice and non-tumor-bearing mice. **i** IHC percentage quantification of NRP2-positive cells in tumor-bearing mice and non-tumor-bearing mice. $n = 6$ samples per group; *, $p < 0.05$; **, $p < 0.01$; ***, $p < 0.005$; error bars present SD

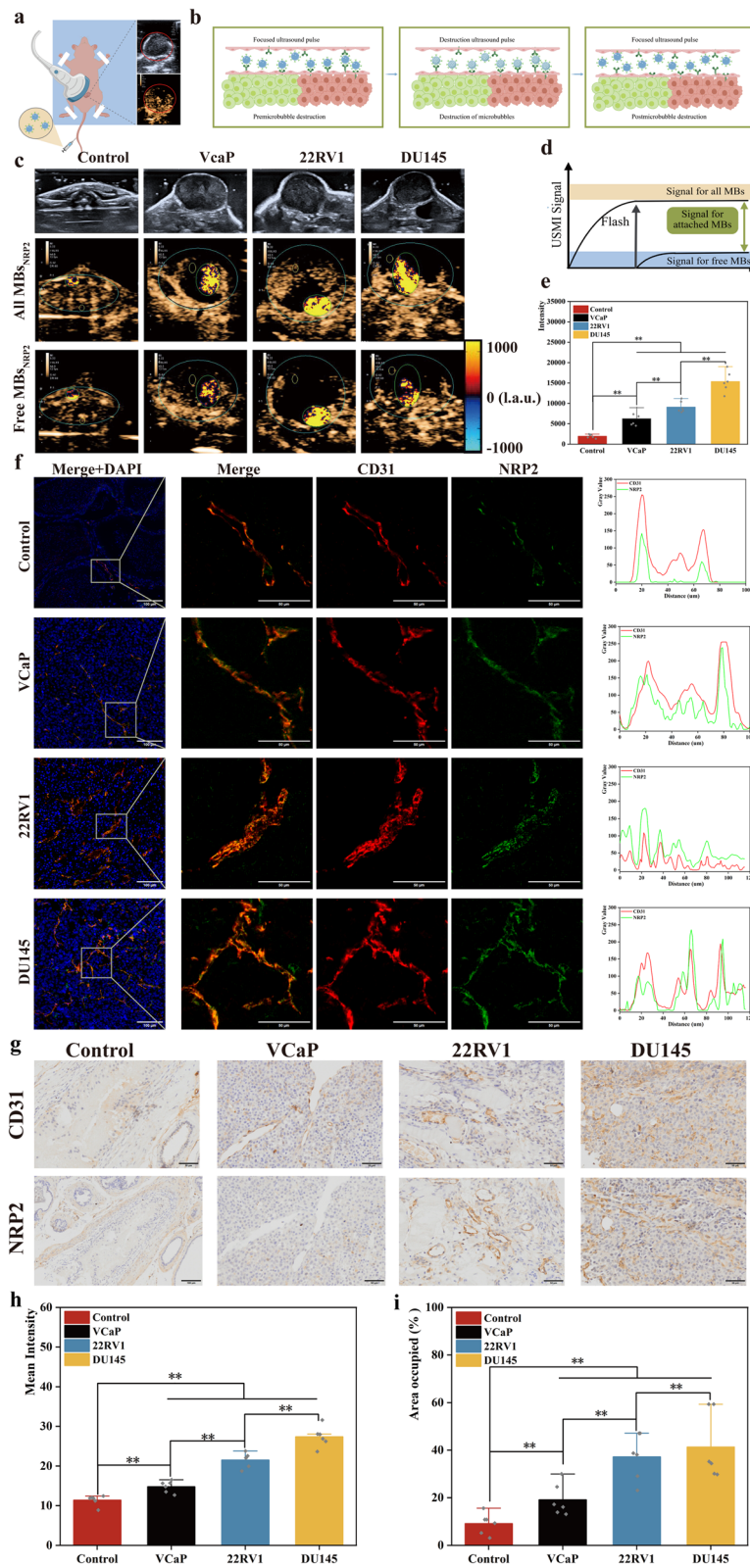


Fig. 6 (See legend on previous page.)

from a normal prostate (mean intensity: 1959.36) is significantly lower ($P < 0.05$) compared with the signal from subcutaneous tumors induced by VCaP cells (mean intensity: 6263.49). The signal from subcutaneous tumors induced by 22RV1 cells (mean intensity: 9110.72) is higher, and the signal from subcutaneous tumors induced by DU145 cells is the highest (mean intensity: 15,356.3). Among these groups, the significant differences in contrast signal intensity observed suggest that NRP2 exhibits differential expression on vascular endothelial cells at different stages of prostate cancer. The difference may be associated with the occurrence and progression of castration resistance in prostate cancer. The findings provide molecular-level evidence for early diagnosis of the development of castration resistance.

Then, the subcutaneous tumors were subjected to *ex vivo* analysis. We performed immunofluorescence staining for NRP2 and further analyzed the colocalization relationship between NRP2 and CD31. The immunofluorescence demonstrated that NRP2 exhibited significant colocalization with CD31, revealing that the NRP2 antibody specifically labels CD31-positive endothelial cells within prostate tumors (Fig. 6f). The semi-quantitative mean fluorescence intensity of normal prostate vascular endothelium was 11.39 a.u., while the mean fluorescence intensity was 14.81 a.u. in the VCaP group, 21.51 a.u. in the 22RV1 group, and 26.56 a.u. in the DU145 group. Significant differences in NRP2 fluorescence intensity were observed among these groups. In other words, the expression of NRP2 on vascular endothelium increases significantly with the progression of prostate cancer, providing molecular-level evidence for the early diagnosis of the onset of castration resistance (Fig. 6g).

Likewise, IHC analysis was also performed on subcutaneous tumors. Due to the vascular restriction of the ultrasound molecular contrast agent, only vascular staining (guided by vascular marker CD31 staining) was quantified. The expression of NRP2 was significantly ($P < 0.05$) higher in DU145 cell tumor-bearing mice (percentage of positive cells, 41.4%) compared with normal tissue (percentage of positive cells, 9.1%), VCaP cell tumor-bearing mice (percentage of positive cells, 19.1%), and 22RV1 cell tumor-bearing mice (percentage of positive cells, 37.2%) (Fig. 6i). In other words, IHC analysis once again confirmed that as prostate cancer resistance progresses, the expression of NRP2 on the corresponding vascular endothelium gradually increases, providing further support for the early diagnosis of the onset of castration resistance.

Based on the resistance status of subcutaneous tumors to an ADT, the ultrasound contrast intensity can be classified into two categories: resistant and non-resistant. Univariable logistic regression was used to analyze the ultrasound contrast signal features, including peak intensity (PI), time to peak intensity (TTP), rise time (RT), rise slope (RS), area under the time-intensity curves (AUC), area under the wedge in curves (winAUC), wedge in rate (winR), fall half time (FHT), mean Transit Time (mTT), fall slope (FS), fall time (FT), area under the wedge out curves (woutAUC), and wedge out rate (WoutR). All variables with $P < 0.05$ in the univariable logistic regression analysis were incorporated into the multivariable logistic regression analysis. As indicated in Table 2, there is a significant statistical difference in peak contrast intensity, which may suggest the occurrence of CRPC. We also utilized the area under the

Table 2 Univariable and multivariable logistic regression analyses of the USMI ($n = 12$)

Variables	Univariable analysis					Multivariable analysis				
	β	S.E	t	P	β (95%CI)	β	S.E	t	P	β (95%CI)
PI	0.01	0.00	6.16	< 0.001	0.01 (0.01 ~ 0.01)	0.01	0.00	5.43	< 0.001	0.01 (0.01 ~ 0.01)
RS	0.01	0.00	3.14	0.005	0.01 (0.01 ~ 0.01)					
TTP	-0.03	0.02	-2.13	0.045	-0.03 (-0.07 ~ -0.01)					
RT	-0.01	0.01	-1.46	0.159	-0.01 (-0.03 ~ 0.01)					
AUC	0.00	0.00	1.31	0.204	0.00 (-0.00 ~ 0.00)					
WinAUC	-0.00	0.00	-0.42	0.678	-0.00 (-0.00 ~ 0.00)					
WinR	0.00	0.00	1.50	0.151	0.00 (-0.00 ~ 0.00)					
FHT	-0.01	0.01	-1.61	0.123	-0.01 (-0.03 ~ 0.00)					
mTT	-0.00	0.00	-1.01	0.325	-0.00 (-0.00 ~ 0.00)					
FS	-0.00	0.00	-1.94	0.065	-0.00 (-0.00 ~ 0.00)					
FT	-0.00	0.01	-0.94	0.358	-0.00 (-0.01 ~ 0.01)					
WoutAUC	0.00	0.00	1.14	0.268	0.00 (-0.00 ~ 0.00)					
WoutR	0.01	0.00	5.36	< 0.001	0.01 (0.01 ~ 0.01)					

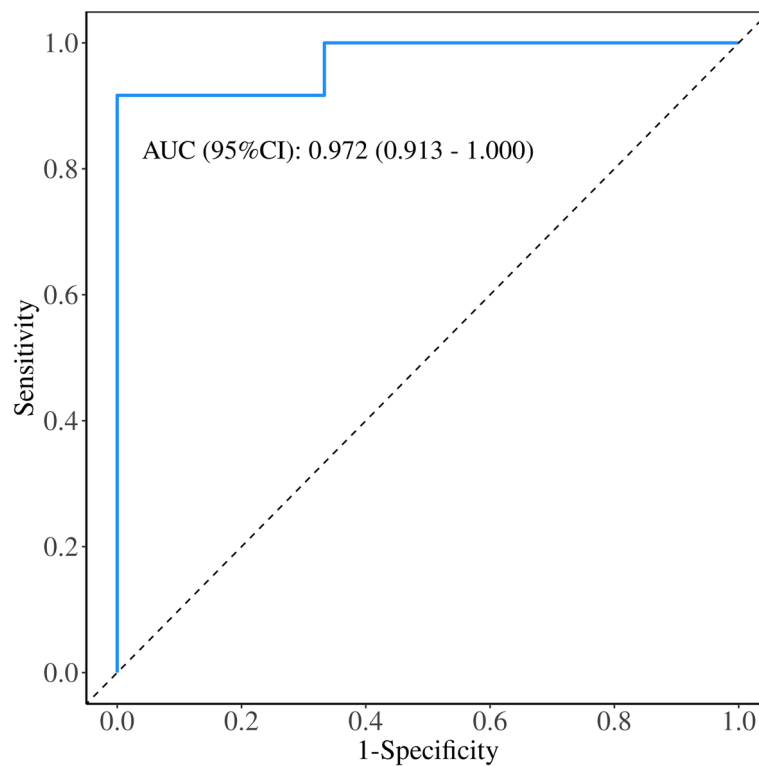


Fig. 7 The ROC curve of the reaction for the PI

receiver-operating-characteristic (AUC) curves (ROC) with 95% confidence intervals (CI) assessed the ability to predict CRPC, with the AUC of 0.972 (CI = [0.913; 1.000]) (Fig. 7).

Discussion

The targets of prostate cancer encompass PSMA, STEAP, DLL3, and so on. These exhibit overexpression on prostate cancer cell membranes, and most related research focuses on targeted therapy for prostate cancer rather than diagnostic directions [41–43]. Similarly, neovascular targets, such as VEGFR, lack specificity when targeting malignant tumor vasculature [44, 45]. VEGFR serves as a neovascularization target, which is highly expressed in malignant prostate cancer vasculature rather than being a unique biomarker for CRPC [46]. CRPC-specific target PSMA, Kluge et al. [47] utilize the area under the receiver-operating-characteristic (AUC) curves (ROC) with 95% confidence intervals (CI) assessed the ability to predict CRPC, with the AUC of 0.737 (CI = [0.609; 0.866]). NRP2, as a marker closely related to neovascularization, has gradually emerged as a candidate target for pathological states characterized by unrestricted vascular dilation, such as cancer [48]. We also utilized ROC with 95% CI assessed the ability to predict CRPC, with the AUC of 0.972 (CI = [0.913; 1.000]). Furthermore, the

expression of the NRP2 protein in the vascular tissues of prostate cancer makes it an attractive new molecular imaging target for prostate cancer [49]. The study confirmed the overexpression of NRP2 in the neovascularization of prostate cancer at three levels: patient samples, co-cultured endothelial cells, and subcutaneous tumor-bearing models. Additionally, NRP2 exhibited distinct differential expression across four stages, namely, normal tissue, HSPC, nmCRPC, and mCRPC, providing a reliable molecular target for differential diagnosis.

Combining novel tumor neovascularization-related markers with control microbubbles to prepare targeted microbubbles, extensive and in-depth research has been conducted in tumor imaging, including breast cancer, colon cancer, ovarian cancer, and so on [10, 50, 51]. These studies aim to provide robust support for molecular imaging, early diagnosis, and differentiation of cancers through precise visualization techniques. Our study utilizes MB_{NRP2} to visualize neovascularization in prostate cancer. Through a parallel-plate flow chamber, simulating the real environment of blood flow shear force, the binding specificity of MB_{NRP2} to vascular endothelial cells in prostate cancer was thoroughly investigated. Specifically, there were significant differences in the number of MB_{NRP2} bound to vascular endothelial cells across four stages: normal prostate tissue, HSPC, nmCRPC, and

mCRPC, showing a gradual increase, which provides a solid experimental basis for USM *in vivo*.

We have also noticed some applications of microbubbles in prostate cancer research. Unfortunately, these studies are primarily confined to their function as an ultrasound contrast agent, which was used to observe the effects of combined therapies on blood flow [50, 52]. Their targeting potential and other roles have not been fully explored. In this study, we utilized the differential expression of the malignant tumor neovascularization marker NRP2 at different stages of prostate cancer (including normal prostate, HSPC, nmCRPC, and mCRPC). By leveraging the specific binding of MBs_{NRP2} to the vascular surface, we aimed to achieve early diagnosis of castration-resistant status through USMI. Specifically, from HSPC to nmCRPC, the number of attached MBs_{NRP2} significantly increased, resulting in a 1.45-fold increase in ultrasound contrast intensity. Similarly, from nmCRPC to mCRPC, the ultrasound contrast intensity increased again by 1.69-fold. The result not only validates the specific binding ability of MBs_{NRP2} to neovascularization in prostate cancer but also provides strong support for the early diagnosis of CRPC.

Indeed, our study has the following limitations. Due to the small size and deep location of the prostate, establishing an orthotopic prostate cancer model is challenging. Subcutaneous tumor models do not accurately reflect the blood supply of the prostate under physiological conditions, thereby limiting the generalizability of our findings. Concerning the constraints posed by subcutaneous tumor-bearing models, we may enhance the approach through the following two methods in our forthcoming research. On one hand, through the establishment of orthotopic tumor models and the creation of genetically engineered mouse models, we strive to align the tumorigenesis and progression more closely with the natural trajectory of prostate cancer, thereby achieving a more precise simulation of the prostate's physiological blood supply [53–55]. On the other hand, integrating organoid models into our research allows us to explore the underlying mechanisms related to physiological blood supply, such as the interplay between prostate cells and vascular endothelial cells [56]. In addition, our study has been somewhat limited by the small sample size and imaging equipment, which resulted in some larger errors. These issues will be addressed in our future research through an increased sample size and the upgrading of imaging equipment.

However, the study confirms that during CRPC progression, there is a significant difference in the USMI intensity generated by attached MBs_{NRP2}, which specifically binds to endothelial cells. Coupled with extensive *in vitro* validation, these findings suggest that targeting

USMI holds great potential in diagnosing CRPC progression, providing valuable experimental support for further research.

In cases where CRPC is clinically suspected, we can conduct USMI based on MBs_{NRP2} and integrate it with existing diagnostic tools like PSA to comprehensively assess the patient's disease condition. Moreover, by combining MBs_{NRP2} with other imaging modalities such as CT and MRI, we can take full advantage of its targeting specificity. This allows us to observe the binding between the receptors on the surface of tumor cells and MBs_{NRP2} with greater precision, thereby furnishing more exhaustive and accurate diagnostic information. Regarding the challenges, first, MBs_{NRP2} must maintain sufficient stability in the body to reach and act on target tumors effectively. However, during circulation, factors like blood flow shear forces and immune cell attacks can destabilize or rupture them, making stability enhancement and prolonged circulation critical technical hurdles. Second, while MBs_{NRP2} is designed to bind specifically to tumor cell receptors, non-specific binding to normal tissues may occur in practice, leading to false positives and reduced diagnostic accuracy. Addressing these issues is essential for reliable clinical application.

Abbreviations

USMI	Ultrasound molecular imaging
PCa	Prostate cancer
HSPC	Hormone-sensitive prostate cancer
nmCRPC	Non metastatic castration-resistant prostate cancer
mCRPC	Metastatic castration-resistant prostate cancer
NRP2	Neuropilin 2
IF	Immunofluorescence
IHC	Immunohistochemistry
WB	Western Blot
CLSM	Confocal laser scanning microscopy
FTIR	Fourier transform infrared
MBs _{Control}	Control microbubbles
MBs _{NRP2}	NRP2-modified microbubbles
TTP	Time to peak intensity
RT	Rise time
RS	Rise slope
AUC	Area under the time-intensity curves
winAUC	Area under the wedge in curves
winR	Wedge in rate
FHT	Fall half time
mTT	Mean transit time
FS	Fall slope
FT	Fall time
woutAUC	Area under the wedge outcurves
woutR	Wedge out rate

Supplementary Information

The online version contains supplementary material available at <https://doi.org/10.1186/s12885-025-14143-7>.

Supplementary Material 1.

Authors' contributions

Na Wang, Xinzhi Xu, and Yizhe Zhong conceived and designed the experiments, performed the experiments, and analyzed the data. Yujie Wan, Ruixia

Hong, and Qizhi Wang prepared figures and tables and authored or reviewed drafts of the article. Jia Tang and Jiaqi Gong performed the experiments and reviewed drafts of the article. Hang Zhou and Fang Li conceived and designed the experiments, authored or reviewed drafts of the article, and approved the final draft. All authors reviewed the manuscript.

Institutional review board statement

The human tissue and animal study was approved by the Institutional Review Board (or Ethics Committee) of Chongqing University Cancer Hospital (protocol code CZLS2024241-A and September 30, 2024).

Funding

This research was funded by NATURAL SCIENCE FOUNDATION OF CHONGQING, CHINA, grant number CSTB2022 NSQC-MSXC324, CSTB2024 NSQC-MSX0647 and CSTB2024 NSQC-MSX0460; FUNDAMENTAL RESEARCH FUNDS FOR THE CENTRAL UNIVERSITIES, grant number 2023 CDJYGRH-ZD02; CHONGQING SCIENCE AND HEALTH JOINT MEDICAL RESEARCH KEY PROJECT, grant number 2025ZDXM015; and CHINA POSTDOCTORAL SCIENCE FOUNDATION, grant number 2023M740439.

Data availability

The data and materials used and/or analyzed during the current study are available from the corresponding author upon reasonable request.

Declarations

Ethics approval and consent to participate

The human tissue study was approved by the Ethics Committee of the Chongqing University Affiliated Cancer Hospital, with the ethics approval number CZLS2025019-A. Our study adhered to the Declaration of Helsinki. Regarding patient informed consent, based on our research protocol, the Ethics Committee of Chongqing University Cancer Hospital has determined that obtaining informed consent from patients is not required. All procedures involving the use of experimental animals were approved by the Ethics Committee of the Chongqing University Affiliated Cancer Hospital, with the ethics approval number CZLS2024241-A.

Consent for publication

Not applicable.

Competing interests

The authors declare no competing interests.

Author details

¹School of Medicine, Chongqing University Cancer Hospital, Chongqing University, Chongqing, China. ²Department of Ultrasound, Chongqing University Cancer Hospital, Chongqing, China.

Received: 30 December 2024 Accepted: 11 April 2025

Published online: 24 April 2025

References

- Siegel RL, Giaquinto AN, Jemal A. Cancer statistics, 2024. *Ca-cancer J Clin*. 2024;74:12–49.
- Pernigoni N, Zagato E, Calcinotto A, Troiani M, Mestre RP, Cali B, et al. Commensal bacteria promote endocrine resistance in prostate cancer through androgen biosynthesis. *Science*. 2021;374:216–24.
- Berruti A, Bracarda S, Caffo O, Cortesi E, D'Angelillo R, Del Re M, et al. nmCRPC, a look in the continuous care of prostate cancer patients: state of art and future perspectives. *Cancer Treat Rev*. 2023;115:102525.
- Fizazi Karim, Shore Neal, Tammela Teuvo L., Ulys Albertas, Vjaters Egils, Pol-yakov Sergey, et al. Darolutamide in Nonmetastatic, Castration-Resistant Prostate Cancer. *New Engl J Med*. 2019;380:1235–46.
- Smith MR, Saad F, Chowdhury S, Oudard S, Hadaschik BA, Graff JN, et al. Apalutamide and Overall Survival in Prostate Cancer. *Eur Urol*. 2021;79:150–8.
- Maha H, Karim F, Fred S, Per R, Neal S, Ubjaraja F, et al. Enzalutamide in Men with Nonmetastatic, Castration-Resistant Prostate Cancer. *New Engl J Med*. 2018;378:2465–74.
- Ilic D, Djulbegovic M, Jung JH, Hwang EC, Zhou Q, Cleves A, et al. Prostate cancer screening with prostate-specific antigen (PSA) test: a systematic review and meta-analysis. *BMJ*. 2018;362:k3519.
- Wischhusen J, Wilson KE, Delcros J-G, Molina-Peña R, Gibert B, Jiang S, et al. Ultrasound molecular imaging as a non-invasive companion diagnostic for netrin-1 interference therapy in breast cancer. *Theranostics*. 2018;8:5126–42.
- Bachawal SV, Jensen KC, Wilson KE, Tian L, Lutz AM, Willmann JK. Breast Cancer Detection by B7–H3–Targeted Ultrasound Molecular Imaging. *Cancer Res*. 2015;75:2501–9.
- Brückner M, Heidemann J, Nowacki TM, Cordes F, Stypmann J, Lenz P, et al. Detection and characterization of murine colitis and carcinogenesis by molecularly targeted contrast-enhanced ultrasound. *World J Gastroenterol*. 2017;23:2899–911.
- Jugnot N, Bam R, Meuliet EJ, Unger EC, Paulmurugan R. Current status of targeted microbubbles in diagnostic molecular imaging of pancreatic cancer. *Bioeng Transl Med*. 2020;6:e10183.
- Johansen ML, Perera R, Abenojar E, Wang X, Vincent J, Exner AA, et al. Ultrasound-Based Molecular Imaging of Tumors with PTPmu Biomarker-Targeted Nanobubble Contrast Agents. *Int J Mol Sci*. 2021;22:1983.
- Klibanov AL. Ultrasound Contrast: Gas Microbubbles in the Vasculature. *Invest Radiol*. 2021;56:50–61.
- Zhong J, Su M, Jiang Y, Huang L, Chen Y, Huang Z, et al. VEGFR2 targeted microbubble-based ultrasound molecular imaging improving the diagnostic sensitivity of microinvasive cervical cancer. *J Nanobiotechnol*. 2023;21:220.
- Ioannidou E, Moschetta M, Shah S, Parker JS, Ozturk MA, Pappas-Gogos G, et al. Angiogenesis and Anti-Angiogenic Treatment in Prostate Cancer: Mechanisms of Action and Molecular Targets. *Int J Mol Sci*. 2021;22:9926.
- Luo Y, Yang Z, Yu Y, Zhang P. HIF1 α lactylation enhances KIAA1199 transcription to promote angiogenesis and vasculogenic mimicry in prostate cancer. *Int J Biol Macromol*. 2022;222:2225–43.
- Melegh Z, Oltean S. Targeting Angiogenesis in Prostate Cancer. *Int J Mol Sci*. 2019;20:2676.
- Tesan T, Gustavsson H, Welén K, Damber J-E. Differential expression of angiotensin-2 and vascular endothelial growth factor in androgen-independent prostate cancer models. *BJU Int*. 2008;102:1034–9.
- Tomić TT, Gustavsson H, Wang W, Jennbacken K, Welén K, Damber J-E. Castration resistant prostate cancer is associated with increased blood vessel stabilization and elevated levels of VEGF and Ang-2. *Prostate*. 2012;72:705–12.
- Unterrainer LM, Calais J, Bander NH. Prostate-specific membrane antigen: Gateway to management of advanced prostate cancer. *Annu Rev Med*. 2024;75:49–66.
- Zhang H, Qi L, Cai Y, Gao X. Gastrin-releasing peptide receptor (GRPR) as a novel biomarker and therapeutic target in prostate cancer. *Ann Med*. 2024;56:2320301.
- Wang M, Wisniewski CA, Xiong C, Chhoy P, Goel HL, Kumar A, et al. Therapeutic blocking of VEGF binding to neuropilin-2 diminishes PD-L1 expression to activate antitumor immunity in prostate cancer. *Sci Transl Med*. 2023;15:eade5855.
- Zhao L, Chen H, Lu L, Wang L, Zhang X, Guo X. New insights into the role of co-receptor neuropilins in tumour angiogenesis and lymphangiogenesis and targeted therapy strategies. *J Drug Target*. 2021;29:155–67.
- Partanen TA, Vuola P, Jauhainen S, Lohi J, Salminen P, Pitkäranta A, et al. Neuropilin-2 and vascular endothelial growth factor receptor-3 are up-regulated in human vascular malformations. *Angiogenesis*. 2013;16:137–46.
- Luo X, He J-Y, Xu J, Hu S-Y, Mo B-H, Shu Q-X, et al. Vascular NRP2 triggers PNET angiogenesis by activating the SSH1-cofilin axis. *Cell Biosci*. 2020;10:113.
- Ahn M-H, Kim J-H, Choi S-J, Kim H-J, Park D-G, Oh K-Y, et al. Neuropilin-2 acts a critical determinant for epithelial-to-mesenchymal transition and aggressive behaviors of human head and neck cancer. *Cell Oncol (Dordr)*. 2024;47:497–511.
- Benwell CJ, Johnson RT, Taylor JAGE, Price CA, Robinson SD. Endothelial VEGFR Coreceptors Neuropilin-1 and Neuropilin-2 Are Essential for Tumor Angiogenesis. *Cancer Res Commun*. 2022;2:1626.

28. Xu Z, Goel HL, Burkart C, Burman L, Chong YE, Barber AG, et al. Inhibition of VEGF binding to neuropilin-2 enhances chemosensitivity and inhibits metastasis in triple-negative breast cancer. *Sci Transl Med*. 2023;15:eadf1128.
29. Liao T, Zhang Y, Ren J, Zheng H, Zhang H, Li X, et al. Noninvasive quantification of intrarenal allograft C4d deposition with targeted ultrasound imaging. *Am J Transplant*. 2019;19:259–68.
30. Wang H, Vilches-Moure JG, Cherkaoui S, Tardy I, Alleaume C, Bettinger T, et al. Chronic Model of Inflammatory Bowel Disease in IL-10-/- Transgenic Mice: Evaluation with Ultrasound Molecular Imaging. *Theranostics*. 2019;9:6031–46.
31. Zhan Y, Zhou F, Yu X, Luo F, Liu F, Liang P, et al. Quantitative dynamic contrast-enhanced ultrasound may help predict the outcome of hepatocellular carcinoma after microwave ablation. *Int J Hyperthermia*. 2019;35:105–11.
32. Li C-X, Lu Q, Huang B-J, Xue L-Y, Yan L-X, Zheng F-Y, et al. Quantitative evaluation of contrast-enhanced ultrasound for differentiation of renal cell carcinoma subtypes and angiomyolipoma. *Eur J Radiol*. 2016;85:795–802.
33. Peng C, Liu L-Z, Zheng W, Xie Y-J, Xiong Y-H, Li A-H, et al. Can quantitative contrast-enhanced ultrasonography predict cervical tumor response to neoadjuvant chemotherapy? *Eur J Radiol*. 2016;85:2111–8.
34. Al-Janabi H, Moyes K, Allen R, Fisher M, Crespo M, Gurel B, et al. Targeting a STING agonist to perivascular macrophages in prostate tumors delays resistance to androgen deprivation therapy. *J Immunother Cancer*. 2024;12:e009368.
35. Qi J, Chen J, von Stillfried S, Kozcera P, Shi Y, Rix A, et al. Molecular ultrasound imaging with clinically translatable cRGD-coated microbubbles to assess $\alpha\beta 3$ -integrin expression in inflammatory bowel disease. *Invest Radiol*. 2024. <https://doi.org/10.1097/RLI.0000000000001143>.
36. Sun Y, Fang J, Shi Y, Li H, Wang J, Xu J, et al. Machine learning based on radiomics features combining B-mode transrectal ultrasound and contrast-enhanced ultrasound to improve peripheral zone prostate cancer detection. *Abdom Radiol (NY)*. 2024;49:141–50.
37. Deng D, Li X, Zhang J-J, Yin Y, Tian Y, Gan D, et al. Biotin-Avidin System-Based Delivery Enhances the Therapeutic Performance of MSC-Derived Exosomes. *ACS Nano*. 2023;17:8530–50.
38. Lu Z, Zhang Y, Wang Y, Tan G-H, Huang F-Y, Cao R, et al. A biotin-avidin-system-based virus-mimicking nanovaccine for tumor immunotherapy. *J Control Release*. 2021;332:245–59.
39. Fallon ME, Mathews R, Hinds MT. In Vitro Flow Chamber Design for the Study of Endothelial Cell (Patho)Physiology. *J Biomech Eng*. 2022;144:020801.
40. Shurbaji S, Al-Ruweidi MKAA, Ali FH, Benslimane FM, Yalcin HC. Application of a Flow-Induced Stress Wave and Investigation of Associated Injuries on Cell Monolayers Using a Parallel Plate Flow Chamber. *Method Protocol*. 2020;3:65.
41. Wang F, Li Z, Feng X, Yang D, Lin M. Advances in PSMA-targeted therapy for prostate cancer. *Prostate Cancer PD*. 2022;25:11–26.
42. Chou J, Egusa EA, Wang S, Badura ML, Lee F, Bidkar AP, et al. Immunotherapeutic targeting and PET imaging of DLL3 in small-cell neuroendocrine prostate cancer. *Cancer Res*. 2023;83:301–15.
43. Bhatia V, Kamat NV, Pariva TE, Wu L-T, Tsao A, Sasaki K, et al. Targeting advanced prostate cancer with STEAP1 chimeric antigen receptor T cell and tumor-localized IL-12 immunotherapy. *Nat Commun*. 2023;14:2041.
44. Liu Z, Wang Y, Huang Y, Kim BYS, Shan H, Wu D, et al. Tumor vasculatures: A new target for cancer immunotherapy. *Trends Pharmacol Sci*. 2019;40:613–23.
45. Patel SA, Nilsson MB, Le X, Cascone T, Jain RK, Heymach JV. Molecular mechanisms and future implications of VEGF/VEGFR in cancer therapy. *Clin Cancer Res*. 2023;29:30–9.
46. Zhang B, Zhao J, Kang D, Wang Z, Xu L, Zheng R, et al. Flubendazole suppresses VEGF-induced angiogenesis in HUVECs and exerts antitumor effects in PC-3 cells. *Chem Biol Drug Des*. 2024;103:e14503.
47. Kluge K, Lotz V, Einspieler H, Haberl D, Spielvogel C, Amereller D, et al. Imaging and outcome correlates of ctDNA methylation markers in prostate cancer: A comparative, cross-sectional [^{68}Ga]ga-PSMA-11 PET/CT study. *Clin Epigenetics*. 2025;17:36.
48. Islam R, Mishra J, Bodas S, Bhattacharya S, Batra SK, Dutta S, et al. Role of neuropilin-2-mediated signaling axis in cancer progression and therapy resistance. *Cancer Metastasis Rev*. 2022;41:771–87.
49. Polavaram NS, Dutta S, Islam R, Bag AK, Roy S, Poitz D, et al. Tumor- and osteoclast-derived NRP2 in prostate cancer bone metastases. *Bone Res*. 2021;9:24.
50. Ge W, Zheng Y, Tao Z. Contrast-enhanced ultrasound analysis of tissue perfusion in tumor-bearing mice following treatment with endostatin combined with radiotherapy. *Exp Ther Med*. 2014;7:1359–63.
51. Willmann JK, Bonomo L, Testa AC, Rinaldi P, Rindi G, Valluru KS, et al. Ultrasound molecular imaging with BR55 in patients with breast and ovarian lesions: First-in-human results. *J Clin Oncol*. 2017;35:2133–40.
52. Lau C, Rivas M, Dinalo J, King K, Duddalwar V. Scoping review of targeted ultrasound contrast agents in the detection of angiogenesis. *J Ultras Med*. 2020;39:19–28.
53. Zhang J, Sud S, Mizutani K, Gyetko MR, Pienta KJ. Activation of urokinase plasminogen activator and its receptor axis is essential for macrophage infiltration in a prostate cancer mouse model. *Neoplasia*. 2011;13:23–30.
54. Zhang Y, Toneri M, Ma H, Yang Z, Bouvet M, Goto Y, et al. Real-time GFP intravital imaging of the differences in cellular and angiogenic behavior of subcutaneous and orthotopic nude-mouse models of human PC-3 prostate cancer. *J Cell Biochem*. 2016;117:2546–51.
55. Kalmuk J, Folaron M, Buchinger J, Pili R, Seshadri M. Multimodal imaging guided preclinical trials of vascular targeting in prostate cancer. *Oncotarget*. 2015;6:24376–92.
56. Waseem M, Wang B-D. Organoids: An emerging precision medicine model for prostate cancer research. *Int J Mol Sci*. 2024;25:1093.

Publisher's Note

Springer Nature remains neutral with regard to jurisdictional claims in published maps and institutional affiliations.